Electronic Supplementary Material (ESI) for Journal of Materials Chemistry A.

Nickel Confined in 2D Earth-abundant Oxide Layers for Highly Efficient and Durable Oxygen Evolution Catalysts

Yayun Pu,[1,2] Matthew J. Lawrence,[1] Veronica Celorrio,[3] Qi Wang,[4] Meng Gu,[4] Zongzhao Sun,[2] Leonardo Agudo Jácome,[5] A.E. Russell,[6] Limin Huang[2*] and Paramaconi Rodriguez[1*]

[1]School of Chemistry, University of Birmingham, Edgbaston, Birmingham B15 2TT, UK

[2]Department of Chemistry, Southern University of Science and Technology, No. 1088 Xueyuan Blvd, Shenzhen, Guangdong 518055, China

[3]Diamond Light Source Ltd, Diamond House, Harwell Campus, Didcot OX11 0DE, UK

[4]Department of Materials Science and Engineering, Southern University of Science and Technology, No. 1088 Xueyuan Blvd, Shenzhen, Guangdong 518055, China
[5]Bundesanstalt für Materialforschung und -prüfung (BAM), Department Materials Engineering, Unter den Eichen 87, 12205 Berlin, Germany

[6]School of Chemistry, University of Southampton, Highfield, Southampton, SO17 1BJ, UK.

*Corresponding author: P.B.Rodriguez@bham.ac.uk, huanglm@sustech.edu.cn

Supporting Information

Experimental

Materials synthesis:

Preparation of $K_{0.45}MnO_2$: The $K_{0.45}MnO_2$ (KMO) was prepared by the solid reaction method.[1-2] K_2CO_3 (99%, Aladdin), Mn_2O_3 (98%, Aladdin) were mixed with the ratio of 0.45:1 and then ground carefully using an agate mortar. The mixture was placed in a crucible and was heated at 800 ^oC for 1 h for decarbonation. After cooling down naturally, the powder was carefully ground and subsequently heated at 800 ^oC for 30 h. The obtained black powder was rinsed with ultrapure water (Milli-Q, 18.4 MΩ cm^{-1}) and dried overnight at 60 ^oC.

Preparation of Ni-exchanged KMO (Ni-KMO): 50 mg of KMO was mixed with 0.5 M $NiCl_2$ solution (20 mL), followed by sonication for 10 min. The resultant suspension was allowed to stand for a given time (10 min, 30 min, 2h, 6 h, 24 h, and 48 h) at room temperature. The powder-solution was separated by centrifugation at 4000 rpm and rinsed with ultrapure water. The process was repeated at least five times. The obtained powder was dried at 50 ^oC overnight.

Preparation of Ni exchanged $H(K)MnO_2$ (Ni-H(K)MO): KMO was reacted with 1 M HCl to extract the K ions. 50 mg of the obtained H(K)MO was mixed with 0.5 M $NiCl_2$ solution (20 mL) followed by sonication for 10 min and thereafter allowed to stand for 24h. The powder-solution was separated by centrifugation at 4000 rpm, washed with ultrapure water and repeated at least five times. The obtained powder was dried at 50 ^oC overnight.

Preparation of Ni-exchanged $HTi_{0.91}O_2$ (Ni-HTO): Layered titanate $HTi_{0.91}O_2$ was prepared using the same method in our previous work.[3] 50 mg of $HTi_{0.91}O_2$ was mixed with 0.5 M $NiCl_2$ solution (20 mL) followed by sonication for 10 min and thereafter allowed to stand for 24 h. The powder-solution was separated by centrifugation at 4000 rpm, washed with ultrapure water and repeated at least five times. The obtained powder was dried at 50 ^oC overnight.

Materials characterizations:

Powder X-ray diffraction (PXRD) was performed on a Bruker D8 Advance X-ray diffractometer with Cu Kα radiation (λ=1.5406 Å) at room temperature. XRD data were recorded between 10^o-50^o with a step size of 0.02^o. X-ray fluorescence spectroscopy (XRF) was performed using a Bruker S8 Tiger 4 kW spectrometer under a He atmosphere. The particle morphology was analyzed by scanning electron microscopy (SEM, Philips XL3 30 environmental (E)SEM instrument) under an accelerating voltage of 15 kV, with Oxford Instruments energy dispersive X-ray spectroscopy (EDS) attachment. The coupled bright field (BF-), high-angle annular dark field scanning transmission electron microscopy (HAADF-STEM) imaging and energy filtered selected area diffraction (EFSAD), a JEOL JEM-2200FS transmission electron microscope TEM, equipped with a field emission gun (FEG), an in-column omega-type energy filtered, Jeol STEM detectors and a Gatan Ultrascan 1000, was operated at an acceleration voltage of 200 kV. For the spatial resolution and distribution of Ni distribution, HAADF-STEM imaging experiments were carried out on a double Cs- corrected FEI Themis G2 operated at an acceleration voltage of 300 kV, coupled with an EDS detector of the type. Thermogravimetry analysis (TGA) was performed in the temperature range of 25-500 ^{o}C by Shimadzu TGA-50 with a heating rate of 10 ^{o}C /min, the nitrogen gas flow was 20 ml/min. X-ray absorption spectroscopy (XAS) measurements were performed on beamline B18 at Diamond Light Source, operating with a ring energy of 3 GeV and at a current of 300 mA.[4] The monochromator comprises Si(311) crystals operating in Quick EXAFS mode. Calibration of the monochromator was conducted using the respective metal foils prior to the measurements. Pellets of the different samples were collected in transmission and fluorescence modes at the Mn K-edge (6539 eV) and Ni K-edge (8332 eV) simultaneously with the foils. The data was analysed using Athena and Artemis programs,[5] which implement the FEFF6 and IFEFFIT codes.[6] X-ray emission spectroscopy (XES) measurements were conducted at Beamline I20-scanning, of Diamond Light Source.[7, 8] The XES spectra have been normalized with respect to their total area using the range 6456-6500 eV.

Electrochemical characterization:

Electrochemical cell setup: All the electrochemical measurements were performed in a three-electrode setup. Before each electrochemical measurement, the electrochemical cell system was stored in permanganate solution overnight. Before testing, the cell was rinsed with ultrapure water and diluted piranha solution to remove permanganate, followed by filling with ultrapure water and heating to ~70 ^{o}C. The hot water was replaced with fresh ultrapure water and reheated five times. Electrochemical measurements were performed by an Autolab PGSTAT100N potentiostat, with Au foil as counter electrode (CE) and Hg/HgO (0.1 M NaOH) as reference electrode (RE), connected via a luggin capillary. The CE was flame annealed and rinsed with water before immersed in electrolyte. Alkaline electrolyte was freshly prepared by dissolution of NaOH beads (Alfa Aesar, semiconductor grade, 99.99%) or KOH pellets in ultrapure water. Concentrations of 1 M, 0.1 M, 0.01 were prepared for pH=14, 13, and 12, respectively. (Alfa Aesar, 99.98%). For pH=8, electrolyte was prepared by adjusting the 0.01 M NaOH solution with $HClO_4$ (Merck KGaA, Suprapur, 70%). The prepared electrolytes were purged with high purity argon for at least 30 min prior to measurements and an Ar stream, acting as a protective layer above the electrolyte, was employed during measurements.

Electrode preparation: Sample powders were dispersed in 5 mL ultrapure water with a concentration of 0.5 mg mL^{-1}, followed by sonication (~30 min) to achieve a good dispersion. Then, 10 μL Nafion D-521 solution (Alfa Aesar, 5% w/w in H_2O and 1-propanol) was added. Glassy carbon (GC) rotating disk electrode (RDE, diameter 5 mm, geometric area = 0.196 cm^{-2}) was polished with 4000 grit wet polish paper to get a fresh surface, following by polishing with 0.5 μm diamond slurry (Kemet) for refining and then rinsed abundantly with ultrapure water. 4 x 20 μL of the prepared ink were drop-casted onto the GC and dried in an oven at 75 ^{o}C to deposit ~0.04 mg catalyst; the loading was ~0.2 mg cm^{-2}.

Cyclic voltammetry (CV): CVs were recorded in a potential window of 0.8 - 1.76 V, with a scan rate of 20 mV s^{-1}. GC RDE was rotated at 1600 rpm to remove generated O_2 bubbles. The Ohmic resistances of the electrochemical system were obtained via positive feedback mode of Autolab PGSTAT100N. To determine the true moles of redox active Ni atoms, integration of the anodic/cathodic waves of the Ni^{2+}/Ni^{3+} couple was performed with varying scan rate. Double layer capacitance was measured in non-Faradaic region between 1.1 - 1.2 V (vs. RHE), with scan rates of 10, 20, 30, 40, 50 60, 70 and 80 mV s^{-1}.

Chronoampermetry: Chronoamperometric measurements were performed after 30 CV cycles, after which the voltammetric profiles became stable. The procedure consisted of an applied potential of 0.8 V for 10 s, followed by electrolysis at a specific OER potential (1.48 V, 1.40 V, 1.38 V or 1.36 V vs RHE) for 3600 s and then back to 0.8 V for 10 s. Long term stability test was the same procedure except keeping at 1.48 V for 10 h.

Calculations:

Mass activity: 1) Ni mass activity, 2) catalyst mass activity were calculated by using the equation of measured current *i* being divided by Ni or catalyst loading *m*:

$$j_{\text{mass}} = \frac{i}{m}$$

Turnover frequency (TOF): the TOF value was calculated by the equation:

$$\text{TOF} = \frac{jS}{4Fn}$$

where j is the measured current density, S is geometric surface area 0.196 cm^2, number 4 means the number of electrons transferred in OER per O_2, F is faradic constant of 96486 C mol^{-1}, n is the moles of active atoms participated in OER. In this work, the active sites are Ni atoms, which can be calculated by integration of pre-OER peak and mass loading from XRF results.

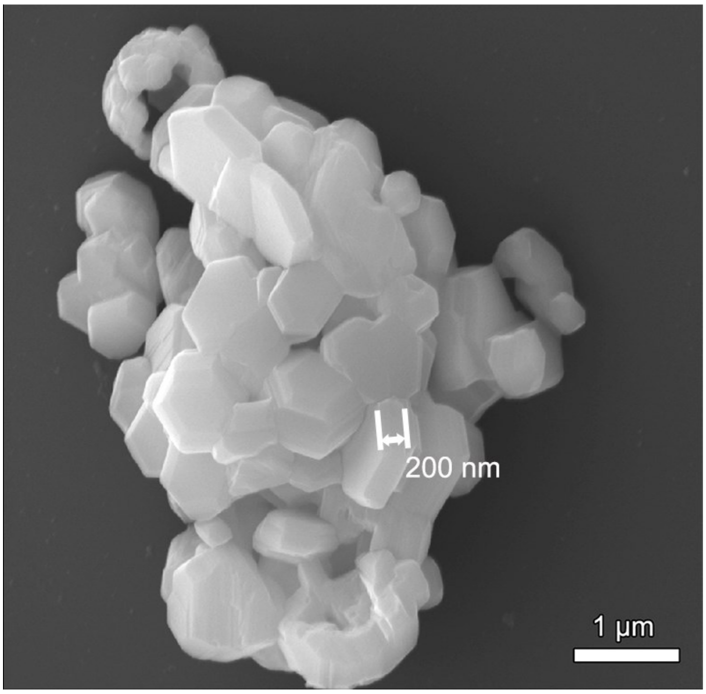

Figure S1. SEM image of $K_{0.45}MnO_2$ nanoparticles synthesized by solid state calcination.

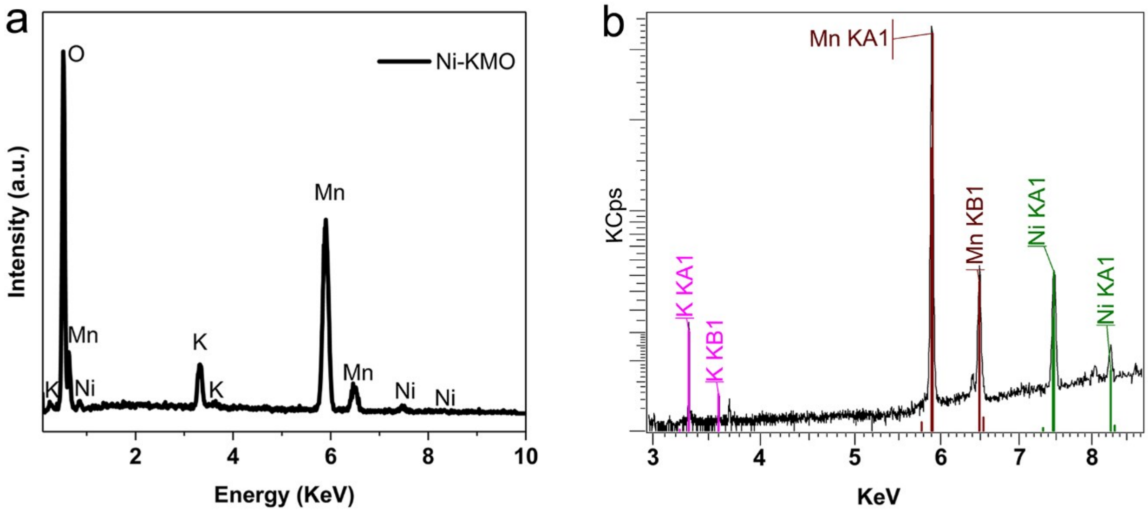

Figure S2. (**a**) STEM-EDS spectrum, (**b**) XRF spectrum.

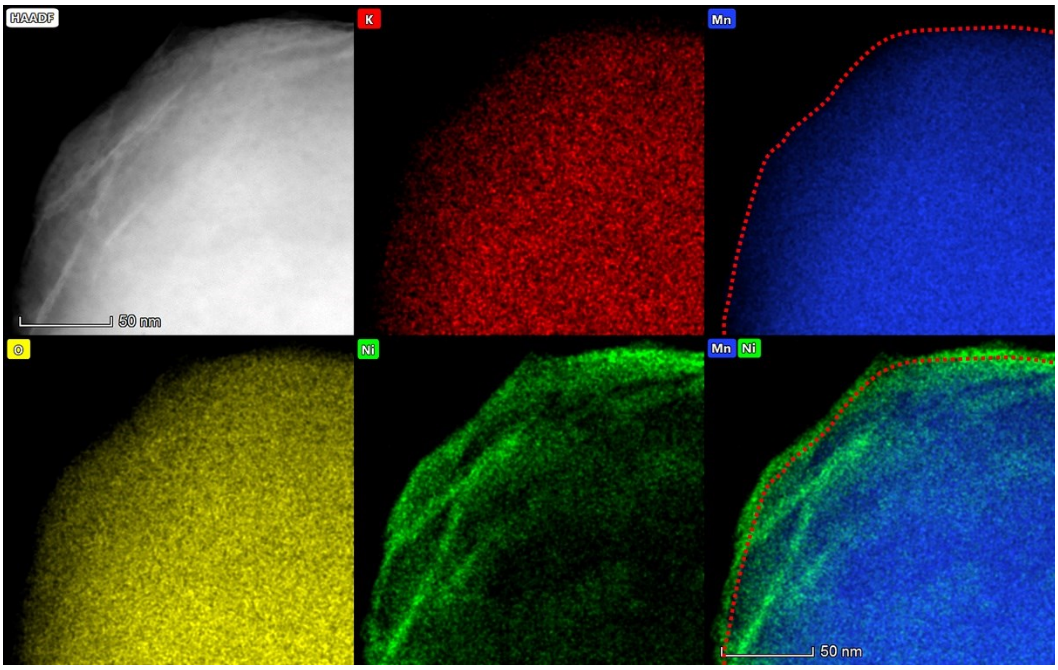

Figure S3. HAADF-STEM EDS elemental mapping of Ni-KMO.

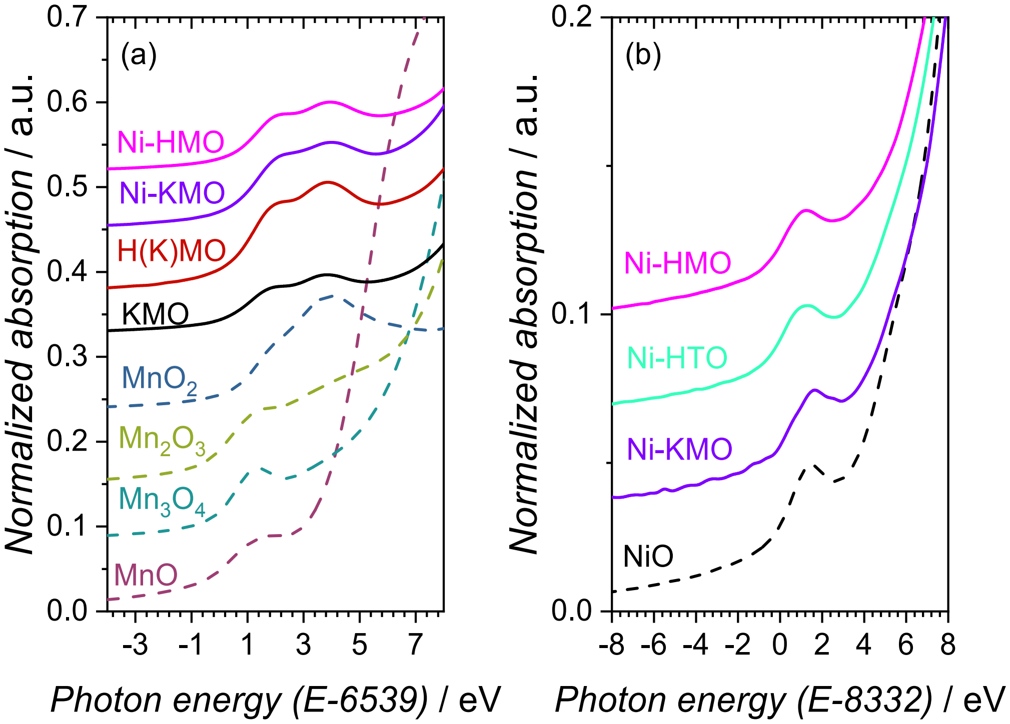

Figure S4. Normalised absorption pre-edge features of X-KMO nanoplates (where M= H or Ni) and oxide reference compounds at (a) Mn K-edge and (b) Ni K-edge. The edge position of the metallic foils, in eV, has been subtracted from the measured spectra presented.

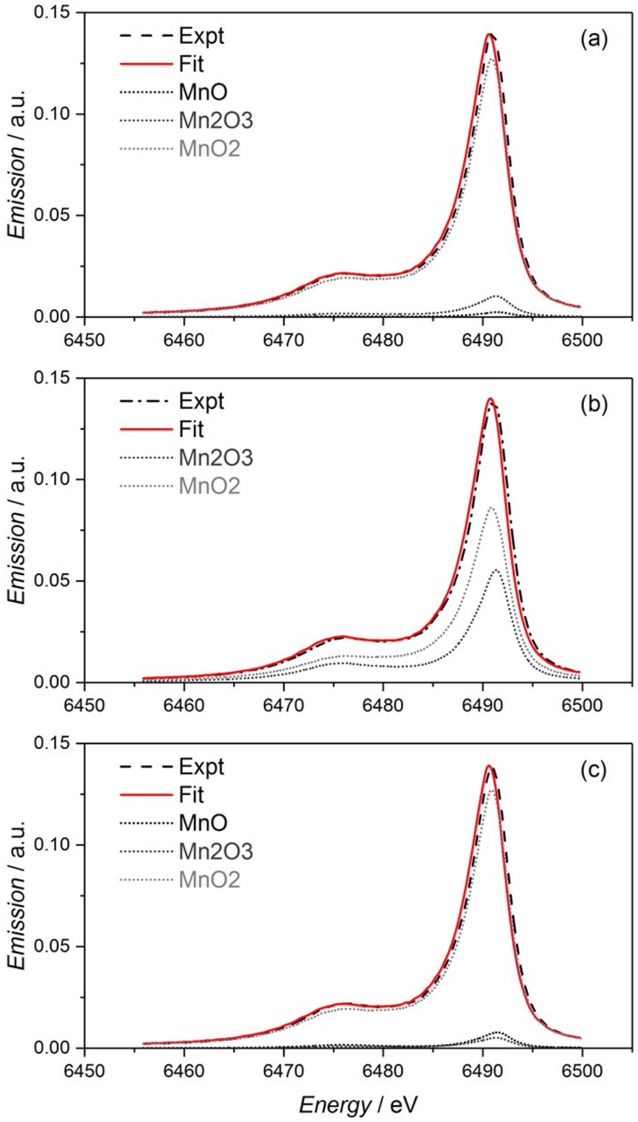

Figure S5. Measured experimental XES spectra of (a) KMO, (b) H(K)MO and (c) Ni-KMO with corresponding fitting contributions from MnO, Mn_2O_3 and MnO_2 standard oxide compounds.

Table S1. Ratio of Mn^{n+} species and corresponding mean Mn oxidation state of prepared KMO derivatives determined by XES.

	% Mn^{4+}	% Mn^{3+}	% Mn^{2+}	Mean Mn oxidation state
KMO	90.5 ± 1.1	7.2 ± 2.7	1.6 ± 1.7	3.9
H(K)MO	61.3 ± 0.9	38.7 ± 0.9	0	3.6
Ni-KMO	90.4 ± 1.2	3.6 ± 2.9	5.1 ± 1.8	3.8

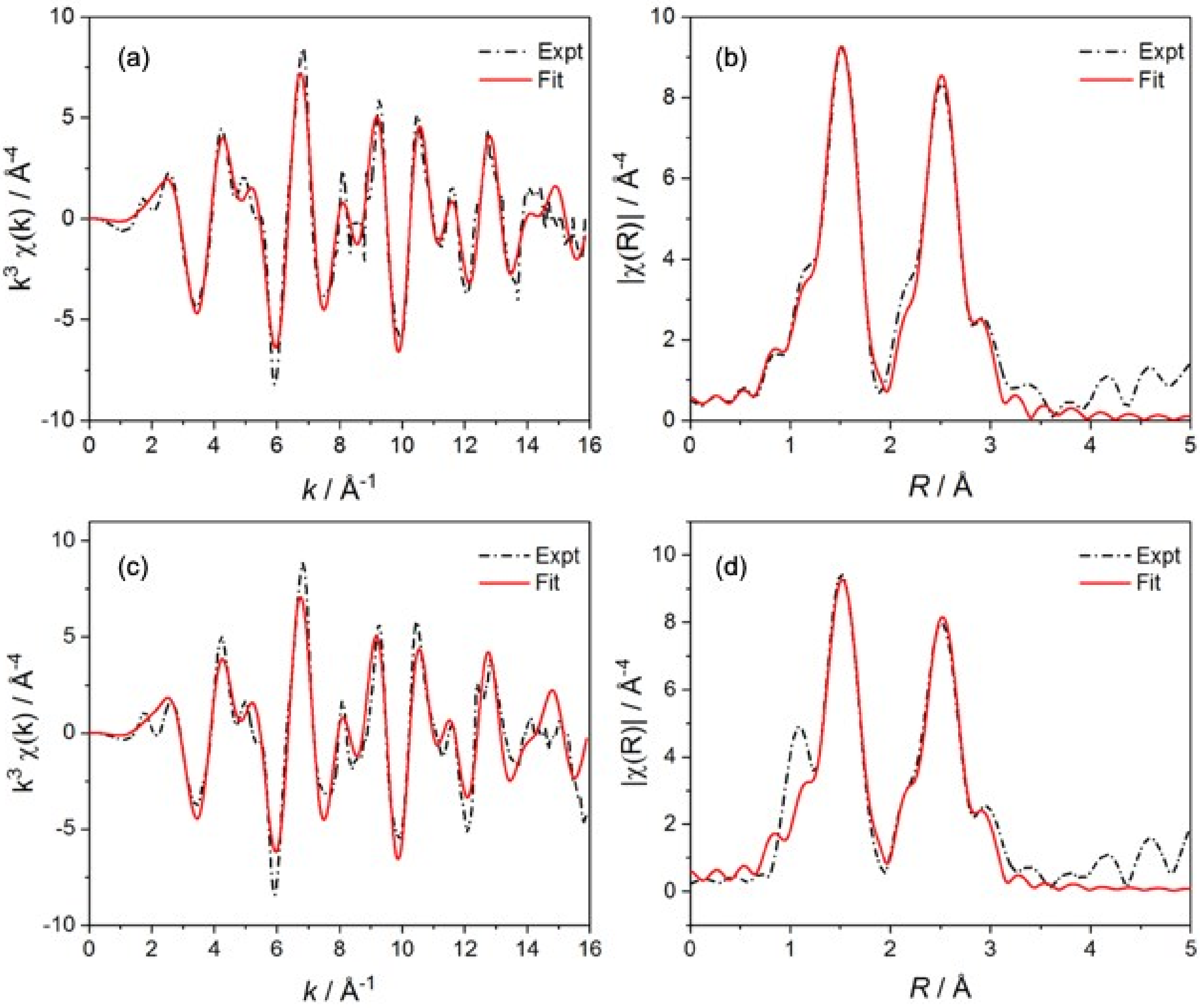

Figure S6. k^3 weighted χ data (a, c) and k^3 weighted Fourier transform EXAFS data (b, d) fits of H(K)MO (*top*) and Ni-KMO (*bottom*).

Table S2. EXAFS distances and fitting parameters for the H(K)MO catalyst. Fitting parameters: $S_0^2 = 0.8$ calculated using a Mn foil standard; fit range $3.0 < k < 13.8$, $1.2 < R < 3.5$. $\Delta E_0 = 0.2 \pm 0.7$ eV; $R_{factor} = 0.008$

Sample	Scattering	CN	R / Å	$\sigma^2 \times 10^3$ / Å^2
H(K)MO	Mn–O	3.3 ± 0.2	1.90 ± 0.01	2.5 ± 0.7
H(K)MO	Mn–Mn_1	5.5 ± 0.8	2.90 ± 0.01	8.2 ± 1.7
H(K)MO	Mn–Mn_2	1.6 ± 0.8	3.14 ± 0.02	4.0 ± 3.4

Table S3. EXAFS distances and fitting parameters for the Ni-KMO catalyst at the Mn K-edge. Fitting parameters: $S_0^2 = 0.8$ calculated using a Mn foil standard; fit range $3.0 < k < 13.9$, $1.2 < R < 3.5$. $\Delta E_0 = 0.5 \pm 0.7$ eV; $R_{factor} = 0.006$

Sample	Scattering	CN	R / Å	$\sigma^2 \times 10^3$ / Å^2
Ni-KMO	Mn–O	2.9 ± 0.2	1.90 ± 0.01	1.8 ± 0.6
Ni-KMO	Mn–$(Ni/Mn)_1$	6.4 ± 0.9	2.91 ± 0.01	9.9 ± 1.7
Ni-KMO	Mn–$(Ni/Mn)_2$	1.6 ± 0.8	3.16 ± 0.02	3.8 ± 3.0

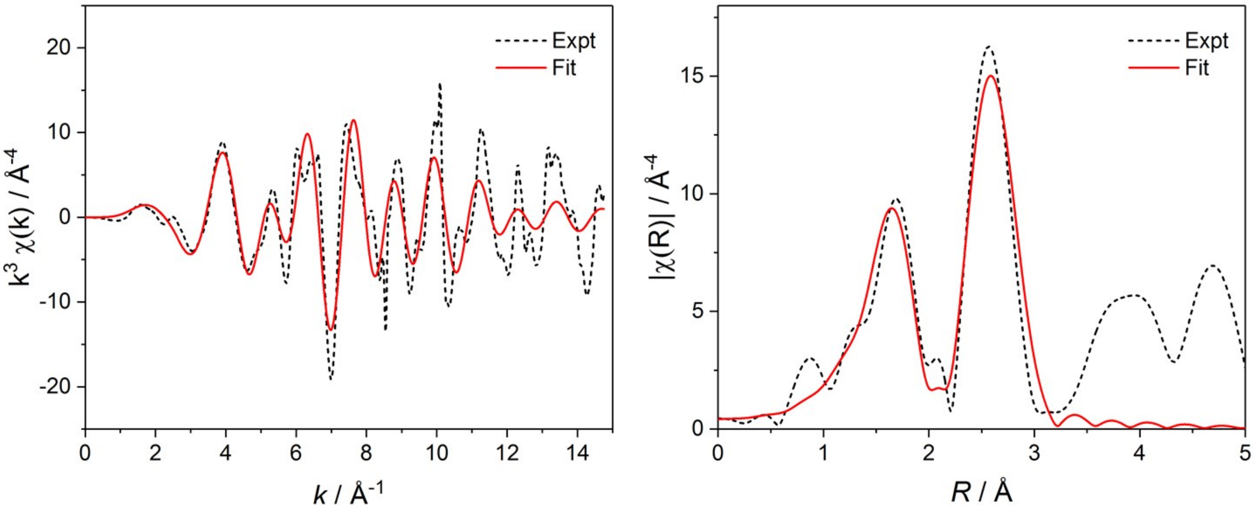

Figure S7. k^3 weighted χ data (left) and k^3 weighted Fourier transform EXAFS data (right) fits for the Ni-KMO catalysts measured at the Ni K-edge.

Table S4. EXAFS distances and fitting parameters for the Ni-KMO catalyst at the Ni K-edge. Fitting parameters: $S_0^2 = 0.8$ calculated using a Ni foil standard; fit range $3.0 < k < 12.1$, $1.0 < R < 3.2$. $\Delta E_0 = -0.4 \pm 1.0$ eV; $R_{factor} = 0.022$

Sample	Scattering	CN	R / Å	σ^2 x 10^3 / Å^2
Ni-KMO	Ni–O	6.9 ± 1.0	2.07 ± 0.01	6.2 ± 2.4
Ni-KMO	Ni–Ni/Mn	12.0 ± 2.3	2.95 ± 0.01	9.2 ± 1.7

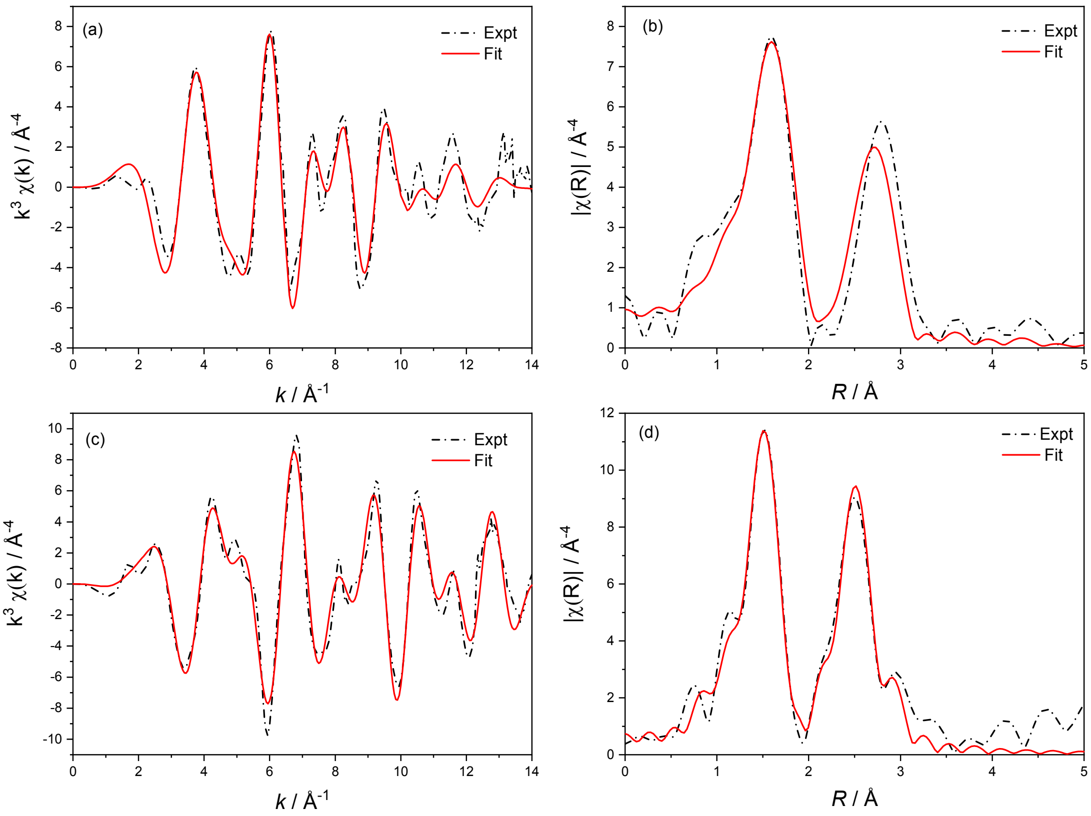

Figure S8. k^3 weighted χ data (left) and k^3 weighted Fourier transform EXAFS data (right) fits for the Ni-HMO catalysts collected at the Ni K edge (a, b) and the Mn K edge (c, d).

Table S5. EXAFS distances and fitting parameters for the Ni-HMO catalyst at the Ni edge. Fitting parameters: $S_0^2 = 0.8$ calculated using a Ni foil standard; fit range $3.2 < k < 12.9$, $1.0 < R < 3.2$. $\Delta E_0 = -4.0 \pm 1.7$ eV; $R_{factor} = 0.027$

Sample	Scattering	CN	R / Å	$\sigma^2 \times 10^3$ / Å^2
Ni-HMO	Ni–O	8.0 ± 1.4	2.06 ± 0.02	9.2 ± 2.6
Ni-HMO	Ni–Ni/Mn	7.0 ± 2.9	3.08 ± 0.03	12.4 ± 4.1

Table S6. EXAFS distances and fitting parameters for the Ni-HMO catalyst at the Mn edge. Fitting parameters: $S_0^2 = 0.8$ calculated using a Mn foil standard; fit range $3.0 < k < 13.9$, $1.2 < R < 3.5$. $\Delta E_0 = -0.1 \pm 0.7$ eV; $R_{factor} = 0.008$

Sample	Scattering	CN	R / Å	$\sigma^2 \times 10^3$ / Å^2
Ni-HMO	Mn–O	4.1 ± 0.2	1.90 ± 0.01	2.7 ± 0.7
Ni-HMO	Mn–(Ni/Mn)$_1$	6.6 ± 1.0	2.90 ± 0.01	9.1 ± 1.9
Ni-HMO	Mn–(Ni/Mn)$_2$	1.7 ± 0.9	3.14 ± 0.03	3.7 ± 3.6

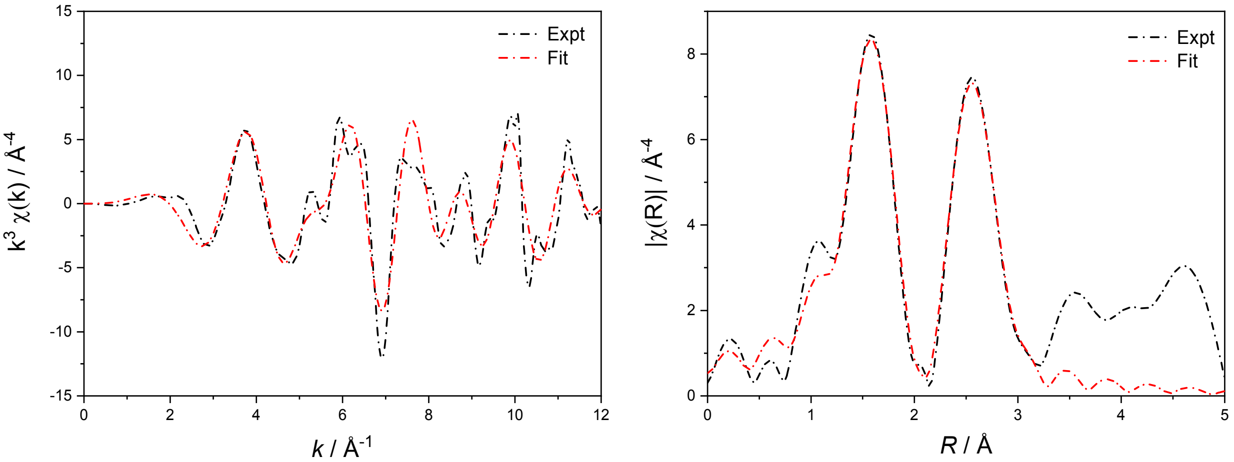

Figure S9. k^3 weighted χ data (left) and k^3 weighted Fourier transform EXAFS data (right) fits for the Ni-HTO catalysts collected at the Ni K edge.

Table S7. EXAFS distances and fitting parameters for the Ni-HTO catalyst at the Ni edge. Fitting parameters: $S_0^2 = 0.8$ calculated using a Ni foil standard; fit range $3.2 < k < 11.1$, $1.0 < R < 3.2$. $\Delta E_0 = -6.4 \pm 0.7$ eV; $R_{factor} = 0.004$

Sample	Scattering	CN	R / Å	σ^2 x 10^3 / Å^2
Ni-HTO	Ni–O	6.6 ± 0.5	2.05 ± 0.01	6.2 ± 1.1
Ni-HTO	Ni–Ni/Ti	4.9 ± 0.8	2.95 ± 0.01	7.5 ± 1.4

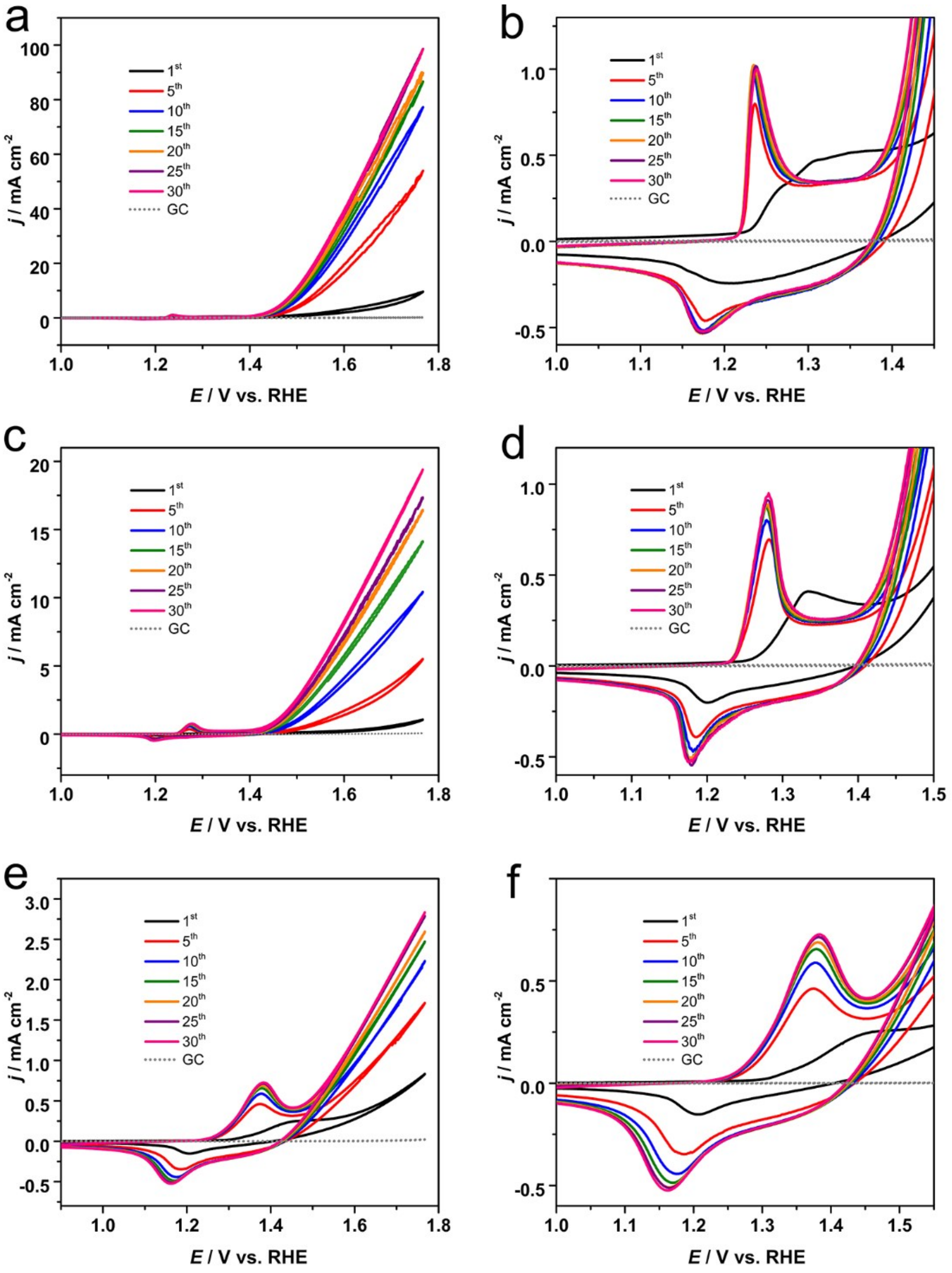

Figure S10. Evolution of Ni-KMO voltammograms (without *iR*-correction) over 30 cycles at (**a**) pH=14, (**c**) pH=13, (**e**) pH=12. Corresponding enlarged redox peaks of $Ni^{2+}/^{3+}$ redox couple at (**b**) pH=14, (**d**) pH=13, (**f**) pH=12.

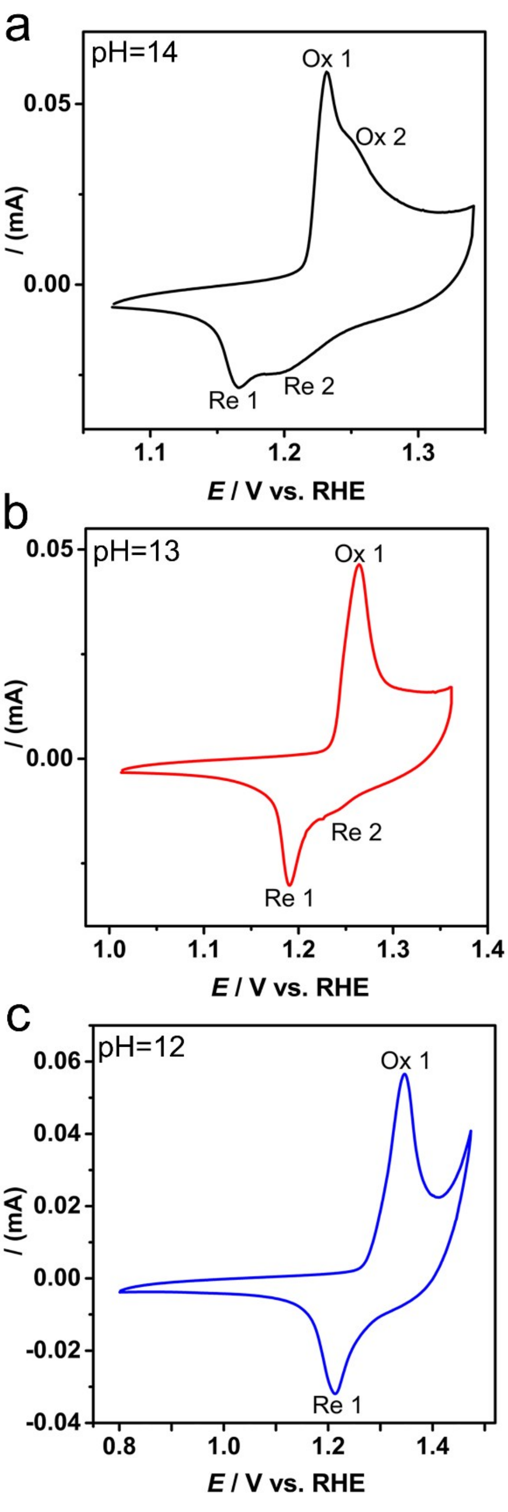

Figure S11. Redox peak correlated NiOOH structure evolution of Ni-KMO at (**a**) pH=14. (**b**) pH=13. (c) pH=12, with scan rate υ = 5 mV s^{-1}.

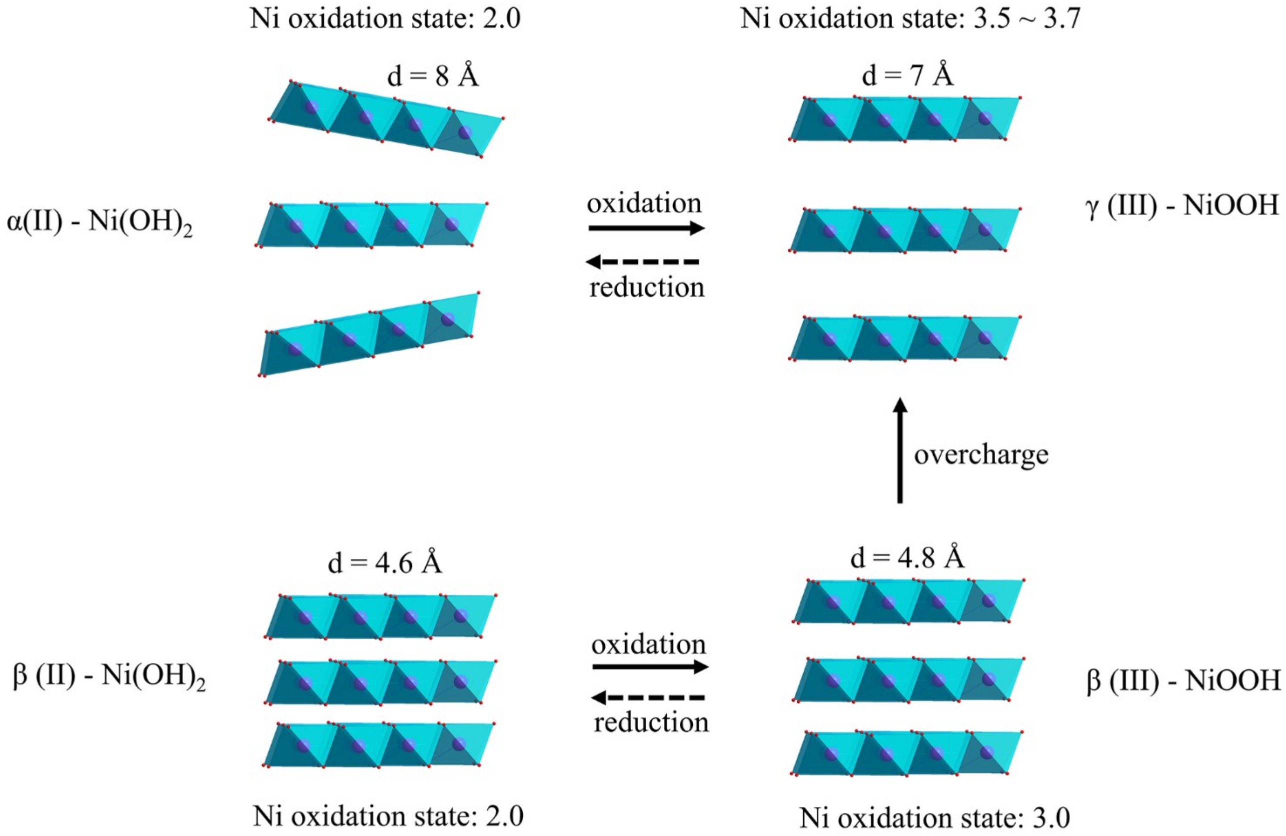

Fig. S12. Schematic graph of Ni based phase transition.[9]

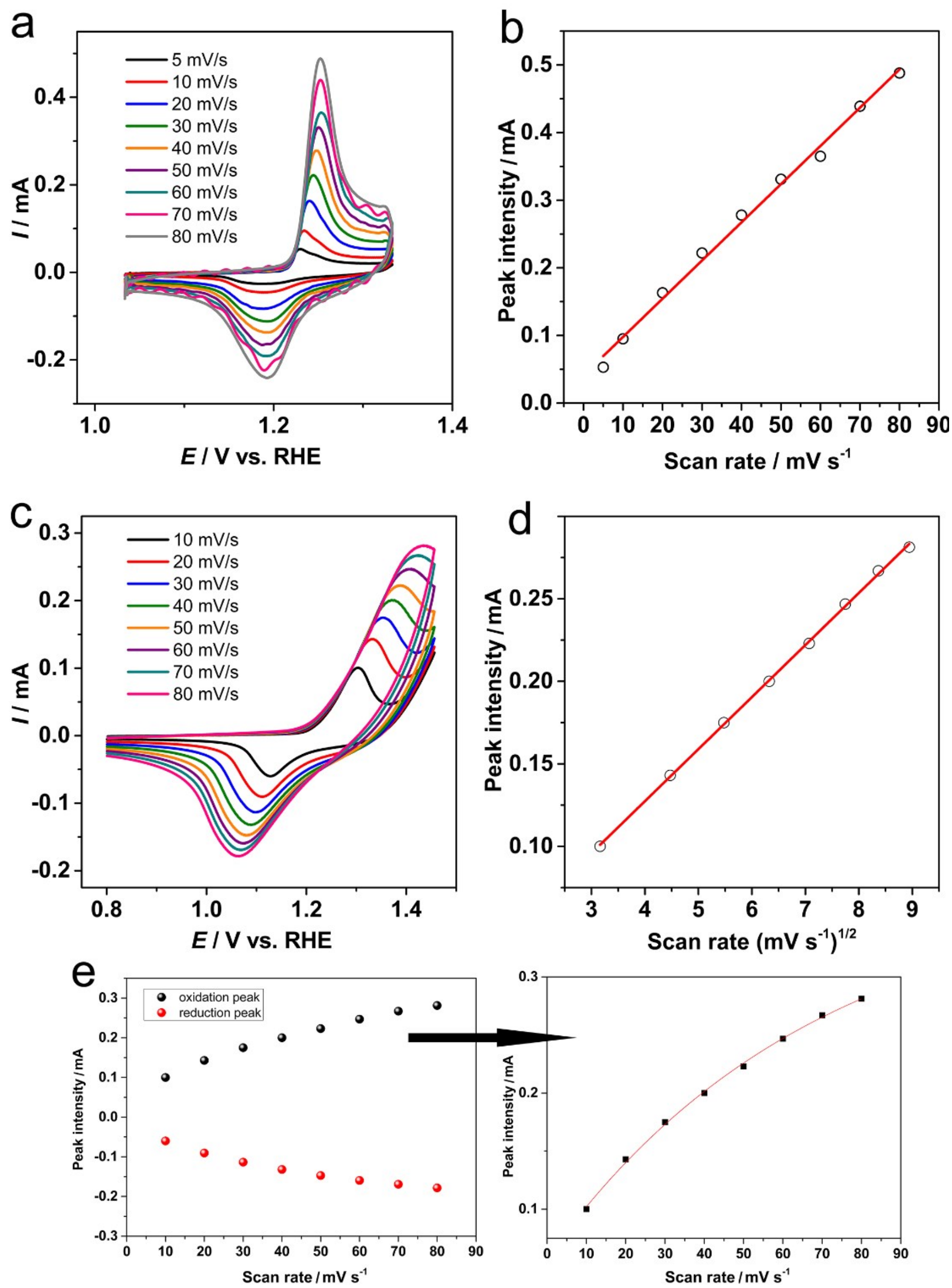

Figure S13. Cyclic voltammograms of Ni-KMO in NaOH, (**a**) $Ni^{2+}/^{3+}$ redox peaks of Ni-KMO with varying scan rates at pH=14, (**b**) corresponding linear fitting of peak value against scan rate. (**c**) $Ni^{2+}/^{3+}$ redox peaks against scan rate of Ni-KMO at pH=12, (**d**) corresponding linear fitting of peak current value against square root of scan rate, (**e**) asymptotic independence of peak currents against scan rate at pH=12.

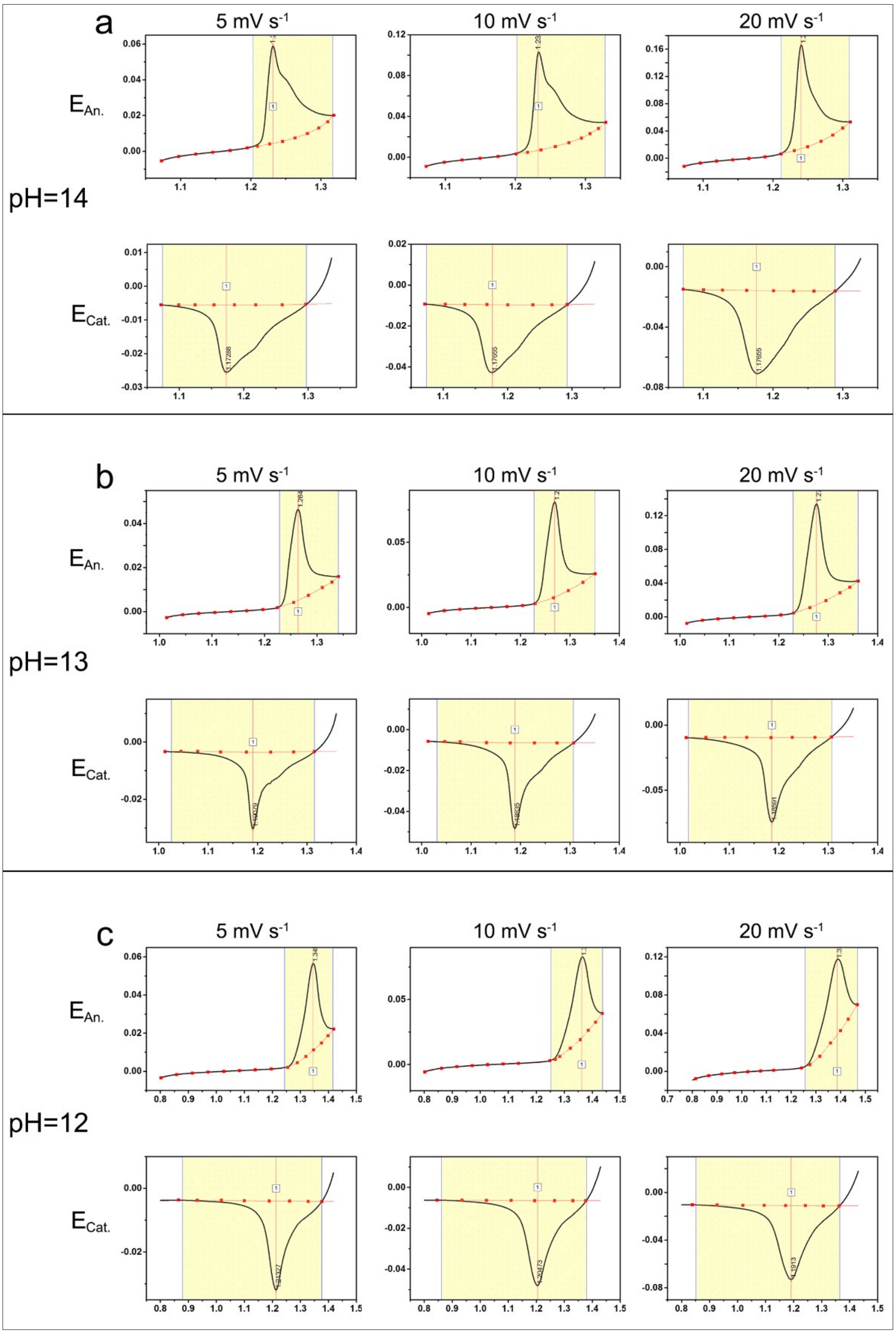

Figure S14. Graphic demonstration of the potential limits and base line for the integration of the charge associated to the Ni redox peaks of Ni-KMO at (**a**) pH=14, (**b**) pH=13, (**c**) pH=12 and different scan rates.

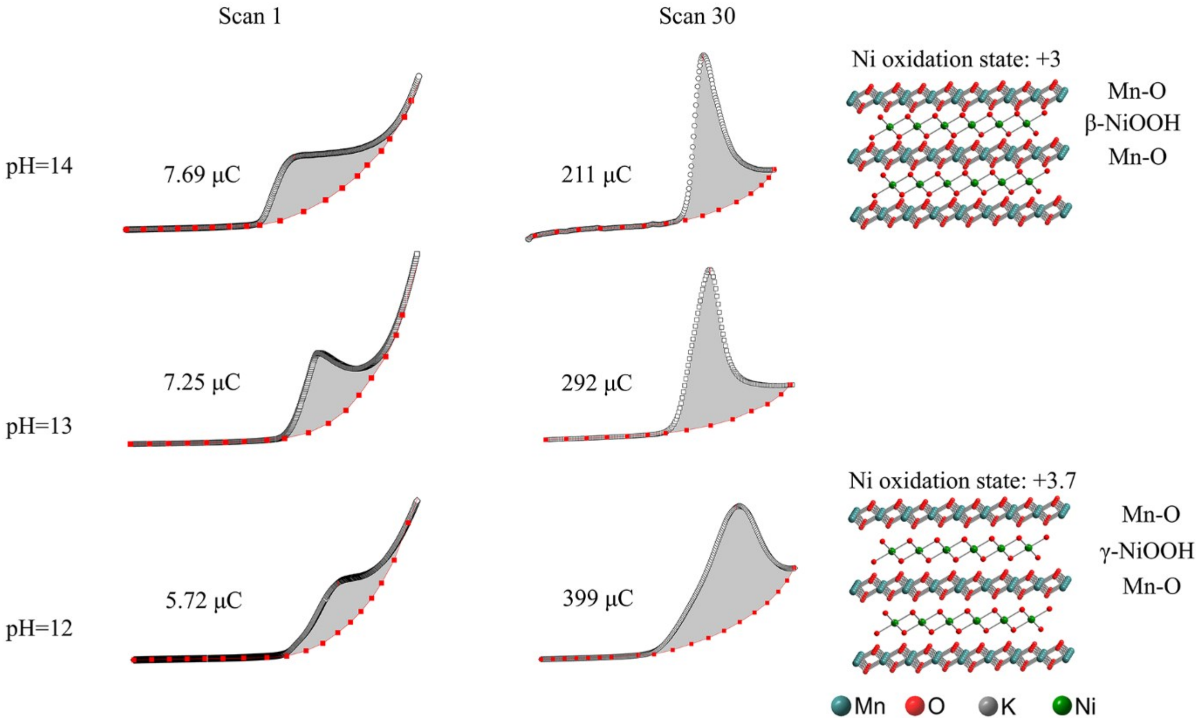

Fig. S15. Integration charge of scan1 and scan 30 at pH=14, pH=13 and pH=12 with the corresponding schematical crystal structures.

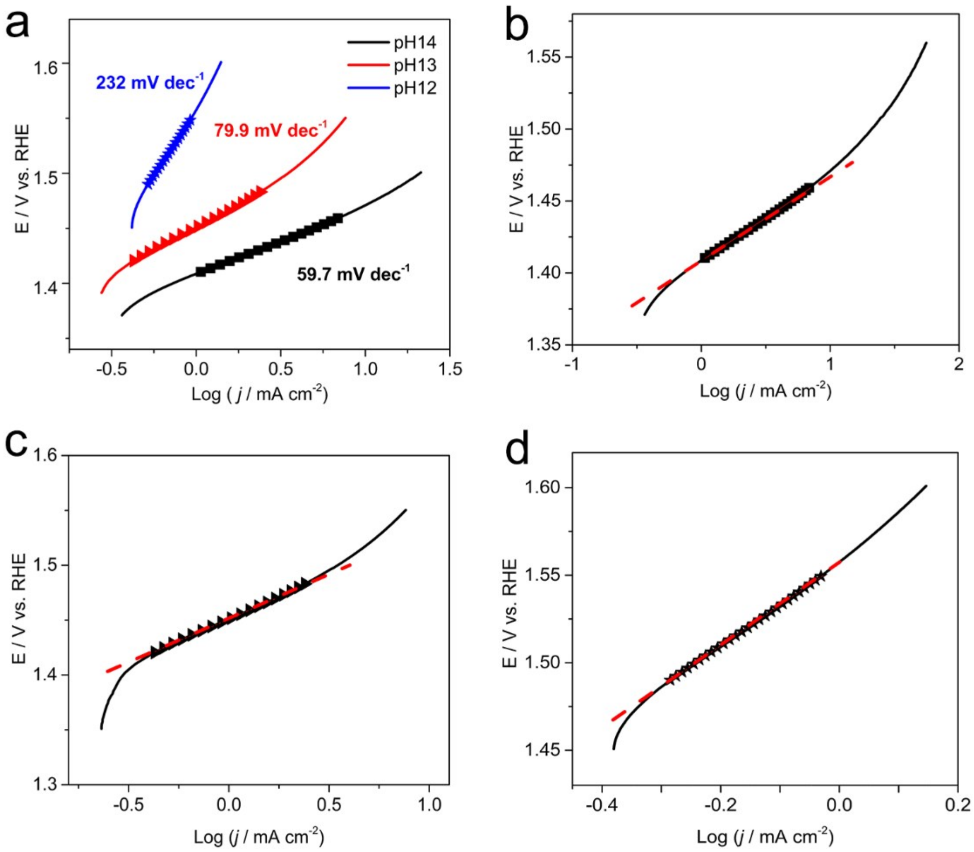

Figure S16. (**a**) Tafel slopes of Ni-KMO, with corresponding slope fitting at (**b**) pH=14, (**c**) pH=13, (**d**) pH=12.

Four electron transfer OER mechanism in alkaline media:

Ni* + OH- → Ni*OH + e- (Eqn. 1)
Ni*OH + OH- → Ni*O + H2O + e- (Eqn. 2)
Ni*O + OH- → Ni*OOH + e- (Eqn. 3)
Ni*OOH + OH- → Ni* + O2 + H2O + e- (Eqn. 4)

The following equation is used for the determination of rate-determining step (RDS) by Tafel slope[10],

$$b = \frac{2.3RT}{a\,F}$$

$$a = \frac{n_f}{v} + n_r\beta$$

R is the gas constant, T is temperature, F is faraday's constant, n_f is the number of electrons transferred before the RDS, v is the stoichiometric number with a typical value of 1, n_r is the number of electrons transferred in a single RDS, β is the symmetry factor with a typical value of 0.5. If the first electron transfer (Eqn. 1) is rate-determining, the Tafel slope can be calculated as 120 mV dec^{-1}. Accordingly, Tafel slopes show values of 40 mV dec^{-1} and 24 mV dec^{-1} as the RDS are the second and the third electron transfer (Eqn. 2 and Eqn. 3), respectively.[11] For the case of Tafel slope of 60 mV dec^{-1}, the RDS involves a chemical step subsequent to the first electron transfer, with $n_r = 0$ and $n_f = 1$. Thus, Ni-KMO at pH=14, RDS is chemical deprotonation; at pH=12, RDS is the adsorption of OH$^-$.

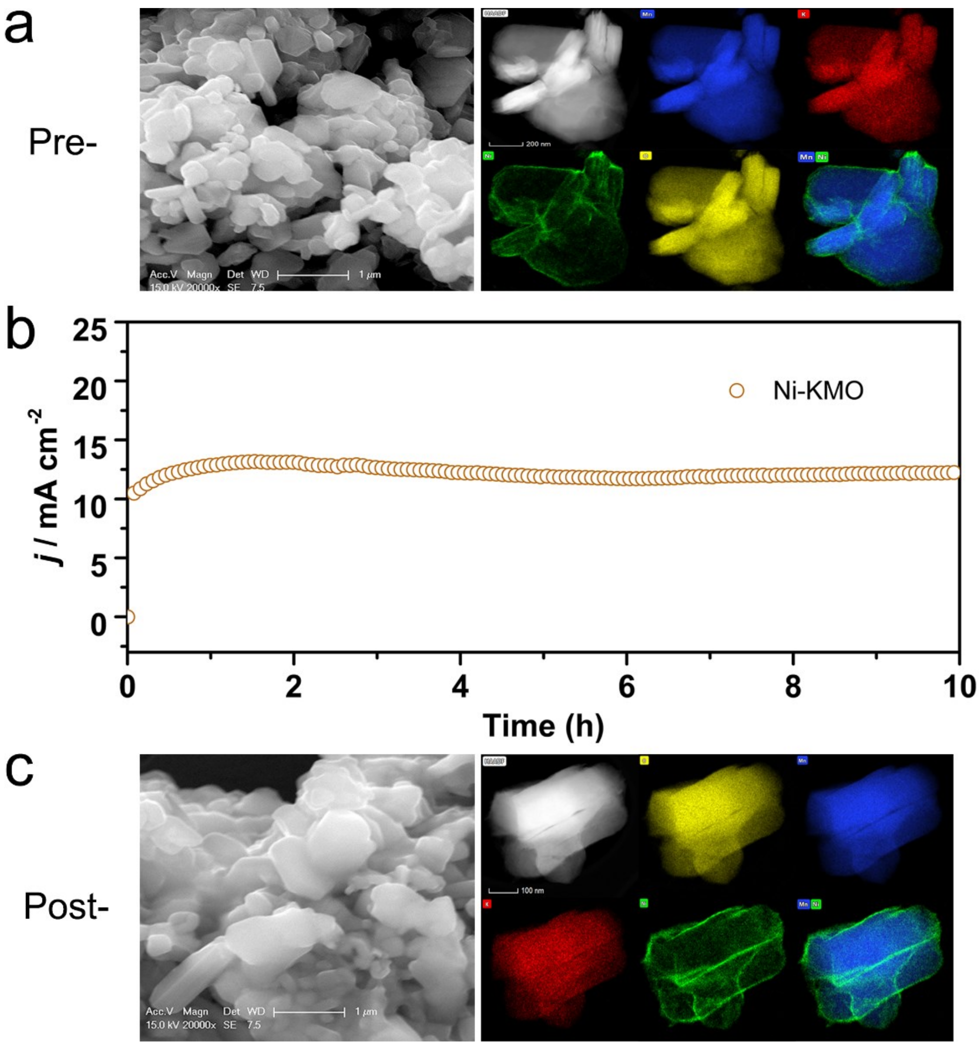

Figure S17. (**a**) SEM and STEM-EDS images of Ni-KMO before electrochemical evaluation, (**b**) chronoamperometry of Ni-KMO at 1.48 V over 10 h, (**c**) SEM and STEM-EDS images of Ni-KMO after electrochemical evaluation.

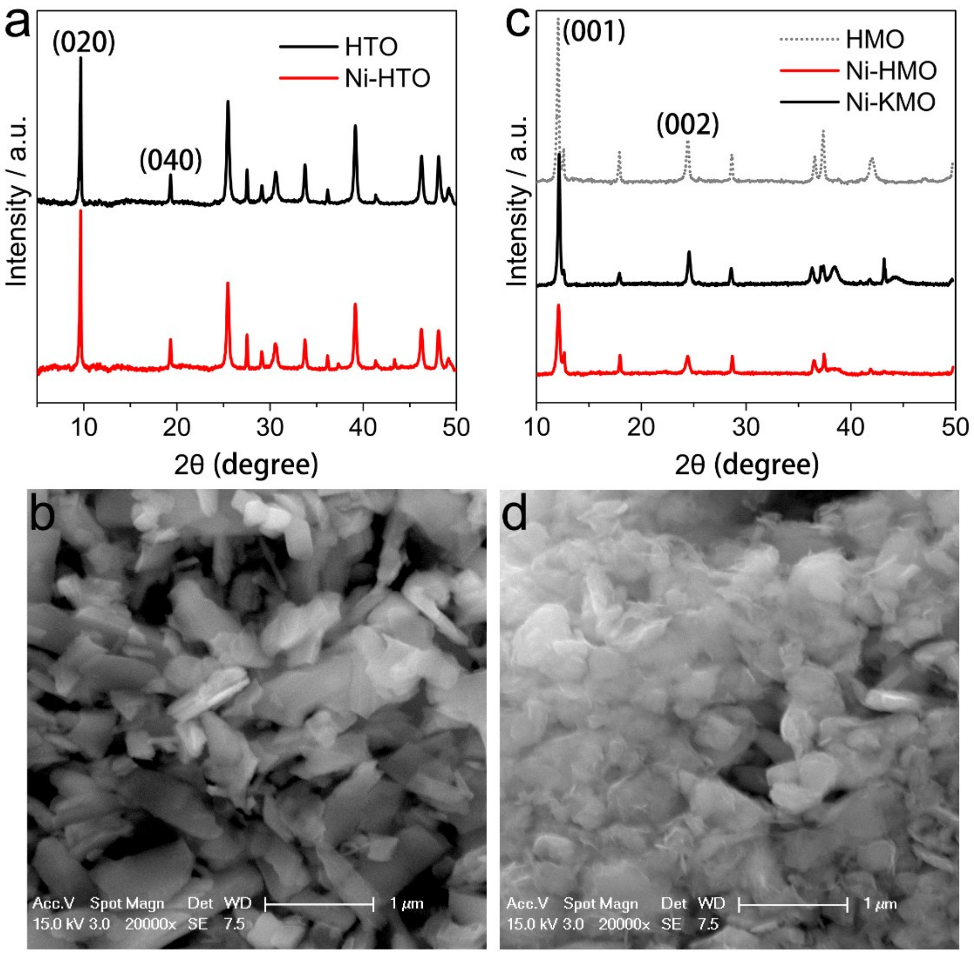

Figure S18. XRD patterns of pristine (**a**) HTO and (**c**) HMO, and after Ni-exchange intercalation. SEM images of (**b**) Ni-HTO, (**d**) Ni-HMO.

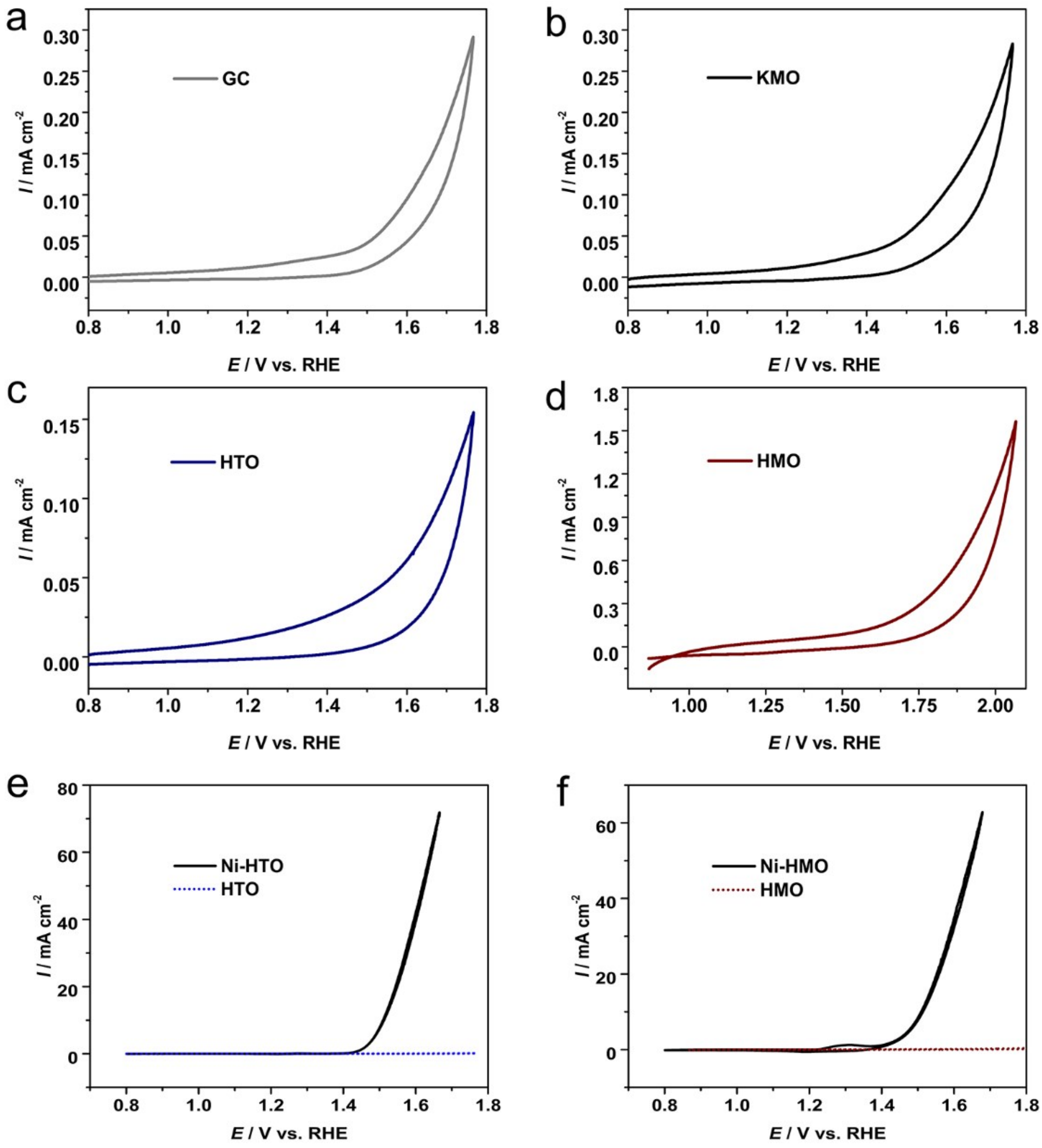

Figure S19. CV of (**a**) GC electrode and pristine (**b**) KMO, (**c**) HTO and (**d**) HMO, (**e**) Ni-HTO and HTO for comparison, (**f**) Ni-HMO and HMO for comparison at pH 14.

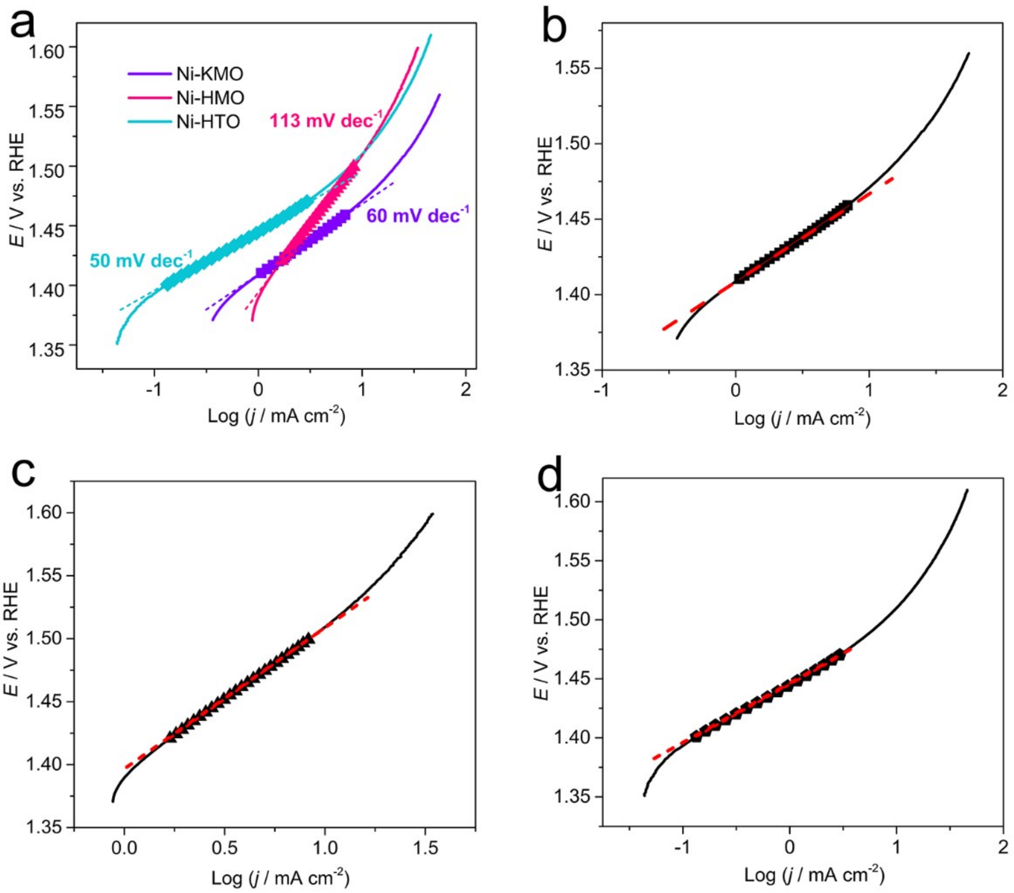

Figure S20. (**a**) Tafel plots of Ni-exchanged layered metal oxides, corresponding fitting of (**b**) Ni-KMO, (**c**) Ni-HMO, (**d**) Ni-HTO at pH=14.

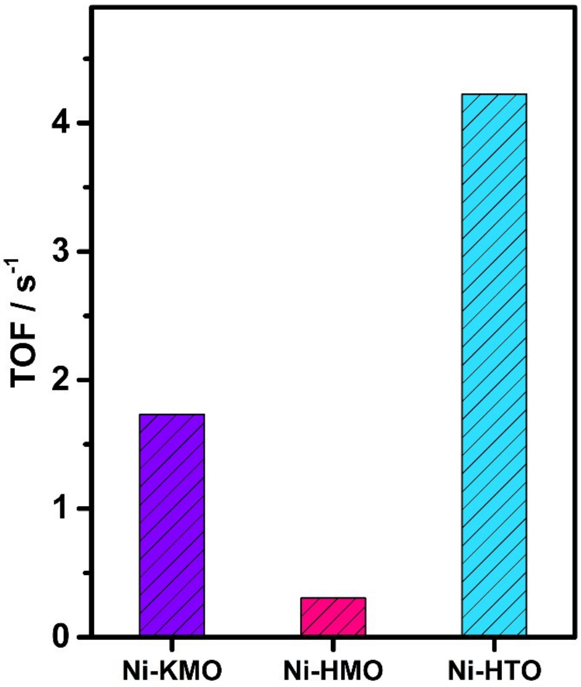

Figure S21. Calculated TOFs normalized by the integrated charge of Ni-exchanged samples at η_{10} = 240 mV.

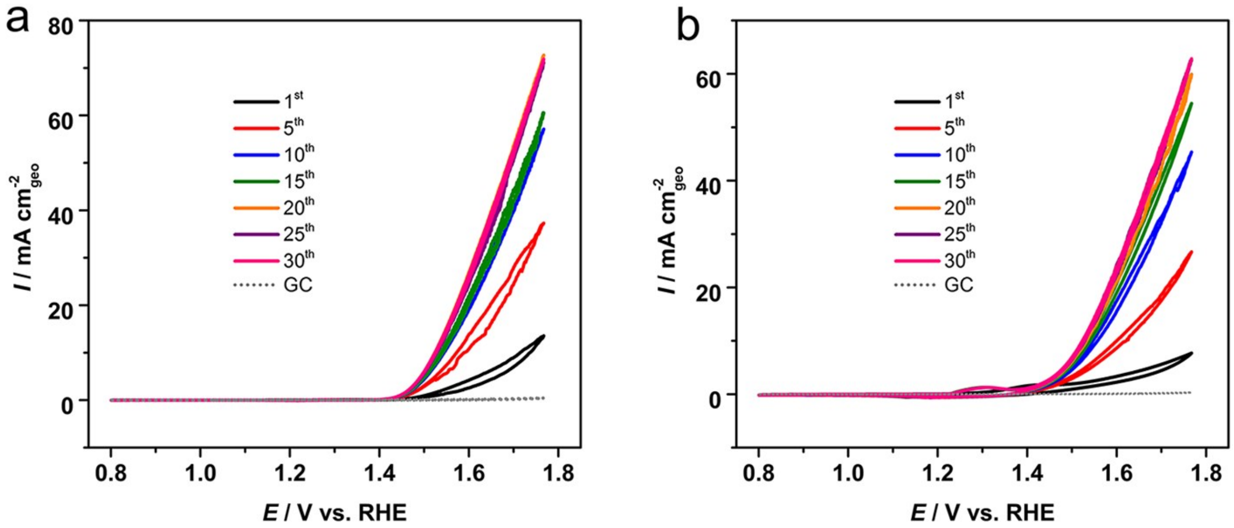

Figure S22. Voltammetric profiles (without *iR*-drop correction) of (**a**) Ni-HTO and (**b**) Ni-HMO evolved in 30 cycles in 1 M NaOH.

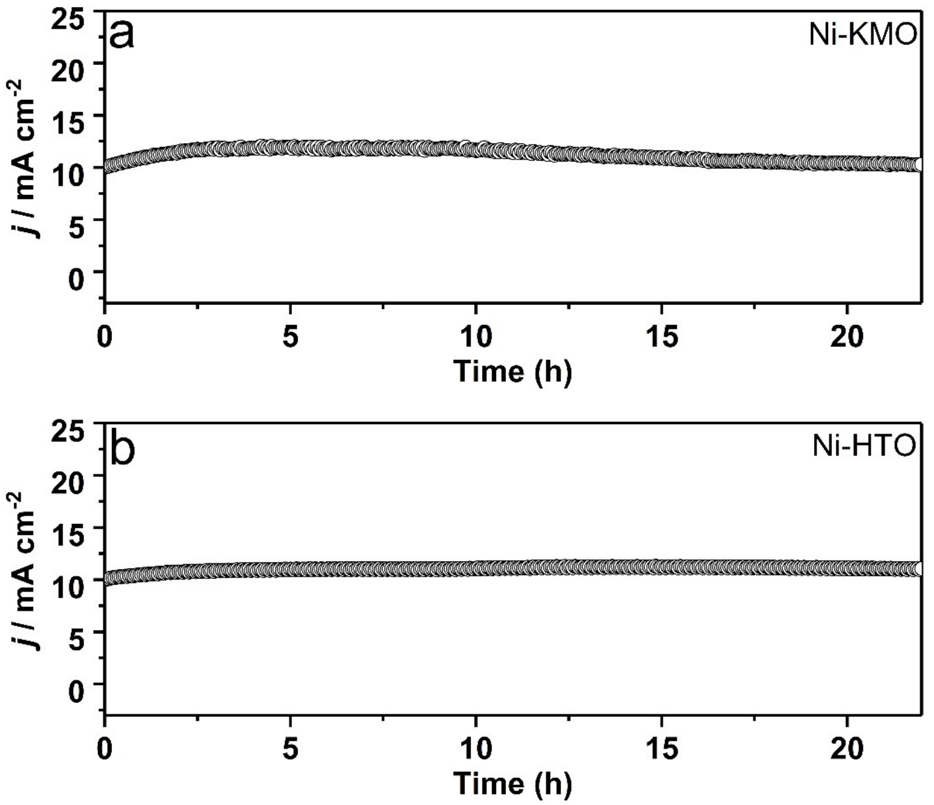

Figure S23. Chronoamperometry of (**a**) Ni-KMO at 1.48 V and (**b**) Ni-HTO at 1.51 V in 1 M NaOH during 23 h.

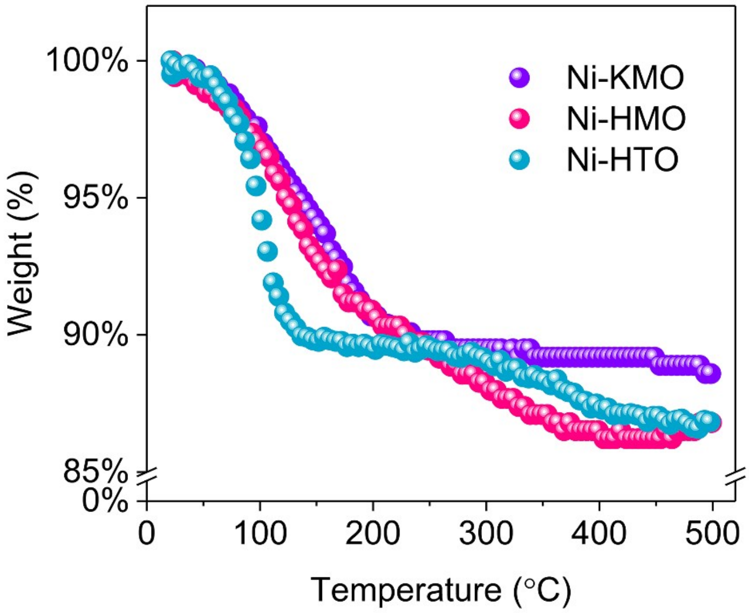

Figure S24. TGA curves of as-synthesized Ni exchanged layered metal oxides.

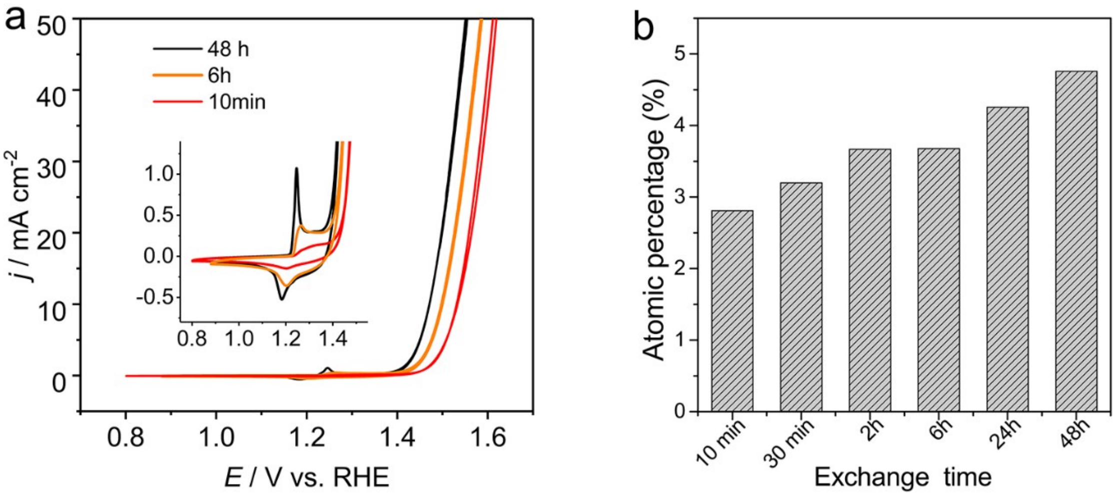

Figure S25. (**a**) Cyclic voltammetry of Ni-KMO with different exchange time in 1 M KOH, scan rate $\upsilon = 20$ mV s^{-1}. Inset show the potential range between 0.8 and 1.5V showing the Ni^{2+}/$^{3+}$ redox peaks (**b**) Ni content of Ni-KMO determined by XRF analysis as a function of the Ni-exchange time.

Table S5. Comparison of mass activity (normalized by active atoms mass) comparison.

	Substrate	Mass activity /A g**-1** Ni	Overpotential /mV	Ref.
Ni-KMO	GC	602	240	This work
Ni-HTO	GC	710	240	This work
$Ni_{3/4}V_{1/4}$ LDH	GC	144	300	Ref[12]
$Ni(OH)_2$	GC	78.4	260	Ref[13]
$Ni_{2/3}Co_{1/3}$ LDH	CP	140	367	Ref[14]
$Ni_{2/3}Fe_{1/3}$ LDH @rGO	GC	93	230	Ref[15]
$NaNi_{0.9}Fe_{0.1}O_2$	GC	168	290	Ref[16]
$Ni_3FeAl_{0.9}$ LDH	GC	33	290	Ref[17]
Au@$Ni_{7/8}Fe_{1/8}$ LDH	Ti mesh	117	280	Ref[18]

Note: GC is glass carbon, CP is carbon paper.

References

1. Omomo, Y.; Sasaki, T.; Watanabe, M., Preparation of protonic layered manganates and their intercalation behavior. *Solid State Ionics* **2002,** *151* (1-4), 243-250.

2. Parant, J.-P.; Olazcuaga, R.; Devalette, M.; Fouassier, C.; Hagenmuller, P., Sur quelques nouvelles phases de formule NaxMnO2 (x⩽ 1). *J. Solid State Chem.* **1971,** *3* (1), 1-11.

3. Pu, Y.; Chen, Q.; Sun, Z.; Rodriguez, P.; Huang, L., Anomalous Phase Transition of Layered Lepidocrocite Titania Nanosheets to Anatase and Rutile. *Cryst. Growth Des.* 2019, 19 (6), 3298-3304.

4. Dent, A. J.; Cibin, G.; Ramos, S.; Smith, A. D.; Scott, S. M.; Varandas, L.; Pearson, M. R.; Krumpa, N. A.; Jones, C. P.; Robbins, P. E., B18: A core XAS spectroscopy beamline for Diamond. *J. Phys.: Conf. Ser.* **2009,** *190*.

5. Ravel, B.; Newville, M., ATHENA, ARTEMIS, HEPHAESTUS: data analysis for X-ray absorption spectroscopy using IFEFFIT. *J. Synchrotron Radiat.* **2005,** *12* (Pt 4), 537-41.

6. Newville, M., EXAFS analysis using FEFF and FEFFIT. *J. Synchrotron Radiat.* **2001,** *8* (2), 96-100.

7. Diaz-Moreno, S.; Amboage, M.; Basham, M.; Boada, R.; Bricknell, N. E.; Cibin, G.; Cobb, T. M.; Filik, J.; Freeman, A.; Geraki, K.; Gianolio, D.; Hayama, S.; Ignatyev, K.; Keenan, L.; Mikulska, I.; Mosselmans, J. F. W.; Mudd, J. J.; Parry, S. A., The Spectroscopy Village at Diamond Light Source. *J. Synchrotron Radiat*. **2018**, *25* (Pt 4), 998-1009.

8. Hayama, S.; Duller, G.; Sutter, J. P.; Amboage, M.; Boada, R.; Freeman, A.; Keenan, L.; Nutter, B.; Cahill, L.; Leicester, P.; Kemp, B.; Rubies, N.; Diaz-Moreno, S., The scanning four-bounce monochromator for beamline I20 at the Diamond Light Source. *J. Synchrotron Radiat*. **2018**, *25* (Pt 5), 1556-1564.

9. Wehrens-Dijksma, M.; Notten, P., Electrochemical quartz microbalance characterization of Ni (OH) 2-based thin film electrodes. *Electrochim. Acta* **2006,** *51* (18), 3609-3621.

10. Guidelli, R.; Compton, R. G.; Feliu, J. M.; Gileadi, E.; Lipkowski, J.; Schmickler, W.; Trasatti, S., Defining the transfer coefficient in electrochemistry: An assessment (IUPAC Technical Report). *Pure Appl. Chem.* **2014,** *86* (2), 245-258.

11. Burke, M. S.; Kast, M. G.; Trotochaud, L.; Smith, A. M.; Boettcher, S. W., Cobalt–iron (oxy) hydroxide oxygen evolution electrocatalysts: the role of structure and composition on activity, stability, and mechanism. *J. Am. Chem. Soc.* **2015,** *137* (10), 3638-3648.

12. Fan, K.; Chen, H.; Ji, Y.; Huang, H.; Claesson, P. M.; Daniel, Q.; Philippe, B.; Rensmo, H.; Li, F.; Luo, Y.; Sun, L., Nickel–vanadium monolayer double hydroxide for efficient electrochemical water oxidation. *Nat. Commun.* **2016,** *7*, 11981.

13. Luan, C.; Liu, G.; Liu, Y.; Yu, L.; Wang, Y.; Xiao, Y.; Qiao, H.; Dai, X.; Zhang, X., Structure effects of 2D materials on α-nickel hydroxide for oxygen evolution reaction. *ACS Nano* **2018,** *12* (4), 3875-3885.

14. Liang, H.; Meng, F.; Cabán-Acevedo, M.; Li, L.; Forticaux, A.; Xiu, L.; Wang, Z.; Jin, S., Hydrothermal Continuous Flow Synthesis and Exfoliation of NiCo Layered Double Hydroxide Nanosheets for Enhanced Oxygen Evolution Catalysis. *Nano Lett.* **2015,** *15* (2), 1421-1427.

15. Ma, W.; Ma, R.; Wang, C.; Liang, J.; Liu, X.; Zhou, K.; Sasaki, T., A Superlattice of Alternately Stacked Ni–Fe Hydroxide Nanosheets and Graphene for Efficient Splitting of Water. *ACS Nano* **2015,** *9* (2), 1977-1984.

16. Weng, B.; Xu, F.; Wang, C.; Meng, W.; Grice, C. R.; Yan, Y., A layered Na1−xNiyFe1−yO2 double oxide oxygen evolution reaction electrocatalyst for highly efficient water-splitting. *Energy Environ. Sci.* **2017,** *10* (1), 121-128.

17. Liu, H.; Wang, Y.; Lu, X.; Hu, Y.; Zhu, G.; Chen, R.; Ma, L.; Zhu, H.; Tie, Z.; Liu, J., The effects of Al substitution and partial dissolution on ultrathin NiFeAl trinary layered double hydroxide nanosheets for oxygen evolution reaction in alkaline solution. *Nano Energy* **2017,** *35*, 350-357.

18. Zhang, J.; Liu, J.; Xi, L.; Yu, Y.; Chen, N.; Sun, S.; Wang, W.; Lange, K. M.; Zhang, B., Single-Atom Au/NiFe Layered Double Hydroxide Electrocatalyst: Probing the Origin of Activity for Oxygen Evolution Reaction. *J. Am. Chem. Soc.* **2018,** *140* (11), 3876-3879.